Characterization of as-deposited cold sprayed Cr-coating on Optimized ZIRLO™ claddings

Journal of Nuclear Materials 549 (2021) 152892

Contents lists available at ScienceDirect

Journal of Nuclear Materials

journal homepage: www.elsevier.com/locate/jnucmat

Characterization of as-deposited cold sprayed Cr-coating on Optimized ZIRLO^{TM} claddings

Andrea Fazi[a,*], Hisham Aboulfadl[a], Anand H.S. Iyer[a], Mohammad Sattari[a], Krystyna Marta Stiller[a], Pratik Lokhande[a,b], Mattias Thuvander[a], Hans-Olof Andren[a]

[a] Department of Physics, Chalmers University of Technology, SE-412 96 Gothenburg, Sweden
[b] Department of Chemistry and Chemical Engineering, Chalmers University of Technology, SE-412 96 Gothenburg, Sweden

ARTICLE INFO

Article history:
Received 28 September 2020
Revised 8 February 2021
Accepted 16 February 2021
Available online 24 February 2021

Keywords:
Accident tolerant fuels
Chromium coatings
Cold spray deposition
Zirconium alloys
Atom probe tomography

ABSTRACT

As-produced Cr-coated Optimized ZIRLO^{TM} cladding material fabricated with the cold-spray (CS) deposition process is studied. Cross-sectional electron microscopy, nano-hardness profiling, transmission electron microscopy, transmission Kikuchi diffraction, and atom probe tomography (APT) were performed to investigate the nature of the CS Cr-coating/Optimized ZIRLO^{TM} interface, the microstructure of the coating, and the effects of the deposition on the Zr-substrate microstructure. The former surface of the Zr-substrate was found to have a highly deformed nano-crystalline microstructure, the formation of which was attributed to dynamic recrystallization occurring during coating deposition. This microstructural change, evaluated with electron backscattered diffraction and nano-hardness profiling, appeared to be confined to a depth of a few microns. Through APT analysis, a 10–20 nm thick intermixed bonding region was observed at the interface between coating and substrate. The chemical composition of this region suggests that this layer originated from a highly localized shearing and heating of a thin volume of the outermost former surface of the substrate. The study of the intermixed bonding region's crystalline structure was performed with high resolution transmission electron microscopy and revealed a distorted hexagonal close-packed structure.

1. Introduction

In 2011, the Fukushima Daiichi accident drew the attention of the nuclear community to the need for accident tolerant fuels (ATFs). Since then, a renewed effort in research for light water reactors (LWRs) is reshaping this technology. The primary focus is to further improve safety measures under design basis accident (DBA) and beyond design basis accident (BDBA) conditions [1,2]. This wave of materials renewal has also created the opportunity to solve or attenuate some of the issues associated with traditional nuclear materials. The work currently being done globally on ATFs is divided between the development of new fuel designs and new cladding designs. In the case of ATF claddings, the main goal is to modify or substitute zirconium alloys to reduce high temperature steam oxidation. Hence, reducing the formation of hydrogen and heat under accident conditions, while possibly also improving resistance to debris fretting, oxidation and corrosion during normal operation [3]. Amongst various proposed ATF cladding concepts, the concept of coated zirconium claddings has emerged as a near term solution, while monolithic FeCrAl alloys and SiC/SiC ceramic composites appear to be the choice for the long term [3]. The application of a coating on zirconium claddings is particularly appealing as it allows to drastically improve high temperature steam oxidation resistance of this component without extensive changes to the design [4]. Metallic chromium coating has been profusely studied and appears to reduce hydrogen pick-up and oxidation rates in pressurized water reactors (PWRs), to enhance the resistance to debris fretting and the mechanical properties of the cladding, therefore making it optimal both during operation and under accident conditions [5–7]. Mainly two deposition methods of this coating are being developed: physical vapour deposition (PVD) coatings [8,9] and cold-spray (CS) deposited coatings [10,11].

The CS technology is a well-established method for coating deposition and deemed to be a good option for the application of corrosion resistant coating on ATF claddings [10]. It involves the expansion of a pre-heated gas to accelerate micro-sized particles of a feedstock powder through a nozzle. The powder is accelerated up to velocities generally ranging between 300 and 1200 m/s [12,13], and high strain-rate plastic deformation occurs upon the collision

* Corresponding author.
E-mail address: fazi@chalmers.se (A. Fazi).

https://doi.org/10.1016/j.jnucmat.2021.152892

of the particles with the substrate. If the particle velocity is above a critical value, the impact will result in the formation of a strong bond between the particle and the substrate [14,15]. The obtained coating/substrate interface is characterised by a strong mechanical interlocking due to the rough topography of the surface and by metallurgical bonding between the periphery of each particle and the substrate or the adjacent particles [16–18]. If compared with chemical vapour deposition (CVD) and PVD, the high deposition rates and the compatibility of CS with deposition at atmospheric pressure are important advantages of this method and allow for its easy application at industrial scale [19]. Unlike in laser deposition or thermal spray deposition, CS deposition does not presume total or partial melting of the feedstock particles. Hence, CS coatings are less affected by oxidation of the feedstock, formation of oxide inclusions, formation of intermetallic compounds or melting/mixing of the substrate surface [20–22]. Nevertheless, the high degree of plastic deformation that characterizes CS technology produces the condition for chemical reactions to occur locally, and can induce phase transformation. These phenomena play an important role for particle adhesion [23–26]. Additionally, when exposed to high temperature, the abovementioned reactions might occur even after the deposition process is complete and this might induce a change in the properties of the component. CS coatings can have residual stresses (caused by the large amount of plastic deformation) and fine grain size in the proximity of the coating/substrate interface or between particles, making the material potentially prone to stress relaxation, recrystallization or grain growth if it is subjected to elevated temperatures [7,27,28].

CS chromium coatings on zirconium alloy claddings have shown excellent adhesion, greatly improved oxidation resistance and decreased hydriding, both in normal operation and in simulated accident environment [7,10,29]. For exposures at 1130 °C or above, the growth of a Cr-Zr intermetallic phase at the coating/substrate interface was reported together with the formation of precipitates in the Zr substrate a few tens of microns below the interface with the coating [7]. These phenomena, in addition to stress relaxation, grain coarsening and recrystallization are typical consequences of heat treatments of CS coatings and are expected to occur even at lower temperatures [27,28,30]. Since CS Cr-coatings are designed to work as ATF in LWRs, the behaviour of such materials in operation and under DBA and BDBA conditions needs to be understood and modelled thoroughly. In order to effectively predict the microstructural evolution of the system and evaluate the ways in which the coating performance is influenced, in-depth characterization of the as-fabricated CS Cr-coated cladding is indispensable.

In this work, the microstructure of as-deposited CS Cr-coated Optimized ZIRLO^{TM} (OPZ) cladding is examined. The atom probe tomography (APT) technique is used for the first time to investigate the chemistry of the CS Cr-coating/Optimized ZIRLO^{TM} interface and the nature of the metallurgical bond between the coating and the Zr-alloy at the nano-scale. The results obtained from APT are compared and validated with high-resolution transmission electron microscopy (HRTEM). Scanning electron microscopy (SEM) and TEM are used to study the microstructure in the proximity of the interface at the micrometre scale, while, electron backscatter diffraction (EBSD) and transmission Kikuchi diffraction (TKD) are employed to map grain size and grain orientation of the same regions. Finally, nano-hardness measurements are utilised to evaluate the depth of the substrate region affected by the coating deposition process.

2. Experimental methods

Pristine CS Cr-coating on OPZ cladding, diameter 10 mm, was provided by Westinghouse Electric Company. The coating was obtained by depositing pure Cr feedstock powder sieved to less than 44 µm in size onto the OPZ (0.8–1.2 wt.% Nb, 0.6–0.79 wt.% Sn, 0.09–0.13 wt.% Fe, 0.09–0.16 wt.% O, balance Zr) cladding, and the achieved particle velocity was 1200 m/s (+/- 50 m/s). A 100 µm thick Cr layer was initially deposited, which was subsequently machined down to 50 µm thickness. From the original tube, rings 5 mm in height were cut with a low-speed diamond saw. The material used for APT and TEM lift-out, was embedded in conductive Bakelite, ground, then polished with SiC-paper and diamond particle suspensions. Samples analysed with SEM, EBSD and nano-hardness measurements were prepared with the use of a broad ion beam (BIB) Leica TIC3X. Cross-sectional SEM images were collected with a JEOL 7800F Prime microscope. Nano-hardness testing was performed with an Alemnis in-situ nanoindenter in a Zeiss Ultra 55 FEG SEM instrument. A cube corner tip was used for good visibility of the indenter tip in the SEM. The indentation experiments were performed in the displacement-controlled mode so that the depth of penetration was close to 100 nm. On the same area, EBSD mapping performed on a TESCAN GAIA3 equipped with Oxford-NordlysNano detector was used to compare the nano-hardness results with the grain microstructure. Lift-outs for TEM and APT analysis were performed using a dual-beam focused ion beam/scanning electron microscopy (FIB/SEM) in a FEI Versa 3D workstation implementing well-known procedures for sample extraction and preparation [31,32]. TEM imaging was carried out on a FEI Tecnai T20 LaB_6 instrument and TKD mapping was conducted to correlate contrast and details in the TEM images with the grain boundaries present in the analysed samples. A LEAP 3000X HR Imago Scientific Instruments was used to collect the APT data. All samples were run in laser mode with 200 kHz laser pulse frequency, at 50–70 K specimen temperature, 0.3 nJ laser pulse energy and 0.20% evaporation rate. CAMECA IVAS 3.6.14 software was used for data reconstruction and data evaluation. HRTEM imaging was performed on a FEI Titan 80–300, operated at 300 kV.

3. Results

3.1. Overall structure of the coating/alloy system

In Fig. 1a an SEM image of a cross-section obtained with BIB is shown. The coating thickness is measured to be around 50 µm; the morphological roughness of the CS-Cr/OPZ interface is relatively high and bulges of chromium wrapped by the substrate can be found protruding into the zirconium. In Fig. 1b a close-up on the interface is presented. Here, it is possible to have a first glimpse at the highly deformed microstructure of the deposited Cr coating, but such information cannot be obtained for the OPZ substrate in this image. Additionally, it is possible to notice a small porosity on the Cr-side (see Fig. 1a), which presents sharp corners that can cause stress-concentration. The Cr/OPZ interface shows clear signs of plastic flow, the zirconium accommodates the Cr-particles by filling the gaps between them. In Fig. 1c, a cross-section milled down with FIB is shown. On this sample, the outer surface of the cladding was ground and polished to reduce the thickness of the coating and allow the region of interest to be imaged clearly using the FIB/SEM. Here, the microstructure of the zirconium substrate is revealed more clearly, so that grains can be recognised by the different shades of grey produced by channelling contrast. The grain structure appears more or less uniform across the imaged area but it becomes much finer in the proximity of the chromium. This finer region seems to extend for approximately 1–2 µm into the substrate. As shown in Fig. 1c, many second phase particles (SPPs) can be found in the substrate. These SPPs are normally expected in OPZ [33] and are visible as dark spots in the image. The different sputter yield values for Cr and Zr under the ion beam are responsible for the curtain effect visible in the lower half of Fig. 1c [34].

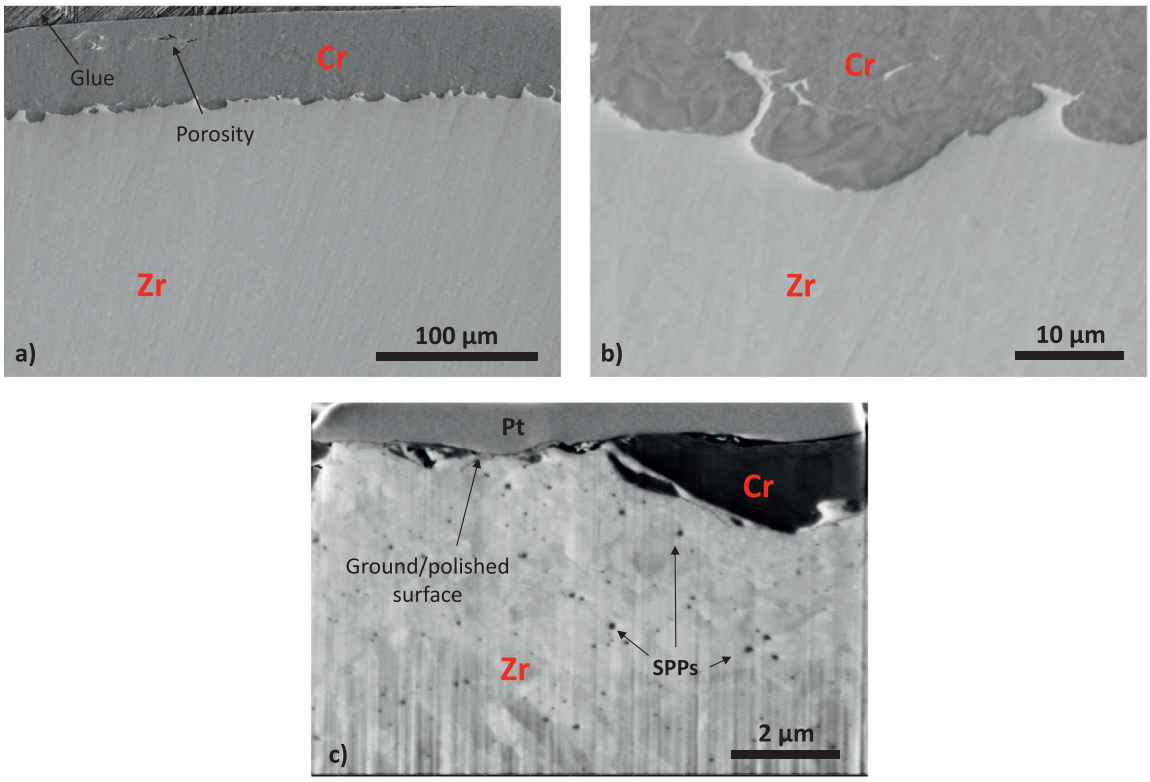

Fig. 1. As-deposited cold sprayed Cr-coated OPZ cladding. Low (a) and high (b) magnification SEM images of cross-section obtained with BIB. (c) SEM image of FIB prepared cross-section.

3.2. Microstructure and deformation of the coating/alloy interfacial region

3.2.1. Nano-hardness measurement

The results of the nano-hardness measurements are presented in Fig. 2a-b. The hardness is displayed as relative hardness, with the substrate hardness set to unity. On average, the chromium coating is harder than the zirconium substrate, with values fluctuating between 1.7 and 3.5 times the substrate hardness. On the other hand, the OPZ hardness reaches 3 times the bulk value in the immediate proximity of the interface, then the hardness decreases sharply in the first micrometre down to 1.5 relative hardness and goes down to the bulk value for distances of 10 µm and beyond.

3.2.2. Electron back scattered diffraction mapping

The results from EBSD analysis are presented in Fig. 3. Fig. 3a shows an overview of the mapped area, while Fig. 3b displays a band contrast map of the same region. The CS-Cr/OPZ interface is delineated by a dark band where almost no point could be indexed. The few Kikuchi patterns collected and indexed in this band were identified as hexagonal Zr, in contrast to the body centred cubic structure identified for the Cr coating. This allows to allocate the CS-Cr/OPZ interface at the top edge of this black region. The microstructure of both OPZ and Cr appears heavily deformed. The Cr presents alternating regions of finer and coarser grain structure that can be associated with inter-particle boundaries and inner-particle regions of the Cr powder particles utilized for the CS deposition. During coating deposition, most of the plastic deformation occurs at the boundary between different powder particles, while the inner-particle regions suffer little plastic deformation. In the OPZ, moving away from the interface, the grain size seems to increase. In approximately the first 10 µm of OPZ only fine grains are found (up to 1 µm grain size). Then, some 3–5 µm sized grains start to appear, still surrounded by micron-sized grains. Starting at this distance the microstructure can be considered unaffected by the deposition process, as it resembles quite well the microstructure of an uncoated OPZ cladding shown in Figs. 3d-e. Two different families of fine grains can be identified in the OPZ substrate. The nano-grains close to the interface, probably formed during the coating deposition, are far below one micron in size. Instead, the fine grains that can be found surrounding the bigger grains in the bulk are characteristic of a partially recrystallized microstructure [35] and have an average size around 1 µm. Overall, the mapped microstructure fits well with the nano-hardness measurements. The alternation of fine and coarse regions in the Cr layer, and small and large grains in the Zr can explain the significant fluctuations in hardness in each area. Fig. 3c shows the pole figures of the basal and prismatic directions (i.e. {0001}and {10$\bar{1}$0}, respectively) for the mapped hexagonal Zr. The OPZ presents a certain degree of texturing, which is usually desired for Zr claddings, hence not surprising [36]. In the analysed sample the prismatic pole points along the axial direction of the cladding tube, while the basal pole seems to be mostly aligned towards the radial direction with a small offset to both sides. The texture seems to be mostly unaffected by the coating deposition.

3.2.3. Bright field transmission electron microscopy and transmission kikuchi diffraction

Bright-field TEM (BF-TEM) images of a lamella lifted-out perpendicularly to the CS-Cr/OPZ interface are presented in Fig. 4. Fig. 4a shows for the most part the Cr side, the interface and a small portion of the OPZ substrate. The Cr grains appear highly deformed with sub-micron average grain size. The grain structure is layered, where plastic deformation and residual stresses can be

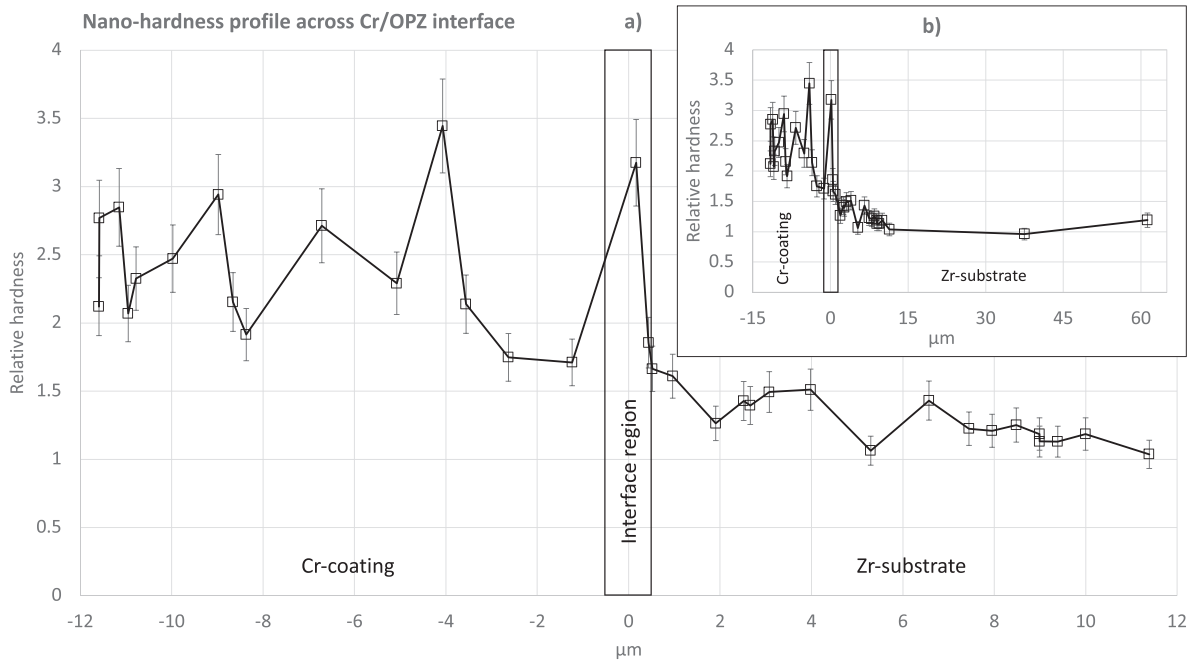

Fig. 2. Nanoindentation measurements on cross-section at the interface between coating and substrate (a), Nano-hardness measurements including two additional measurements in the bulk of the substrate (b).

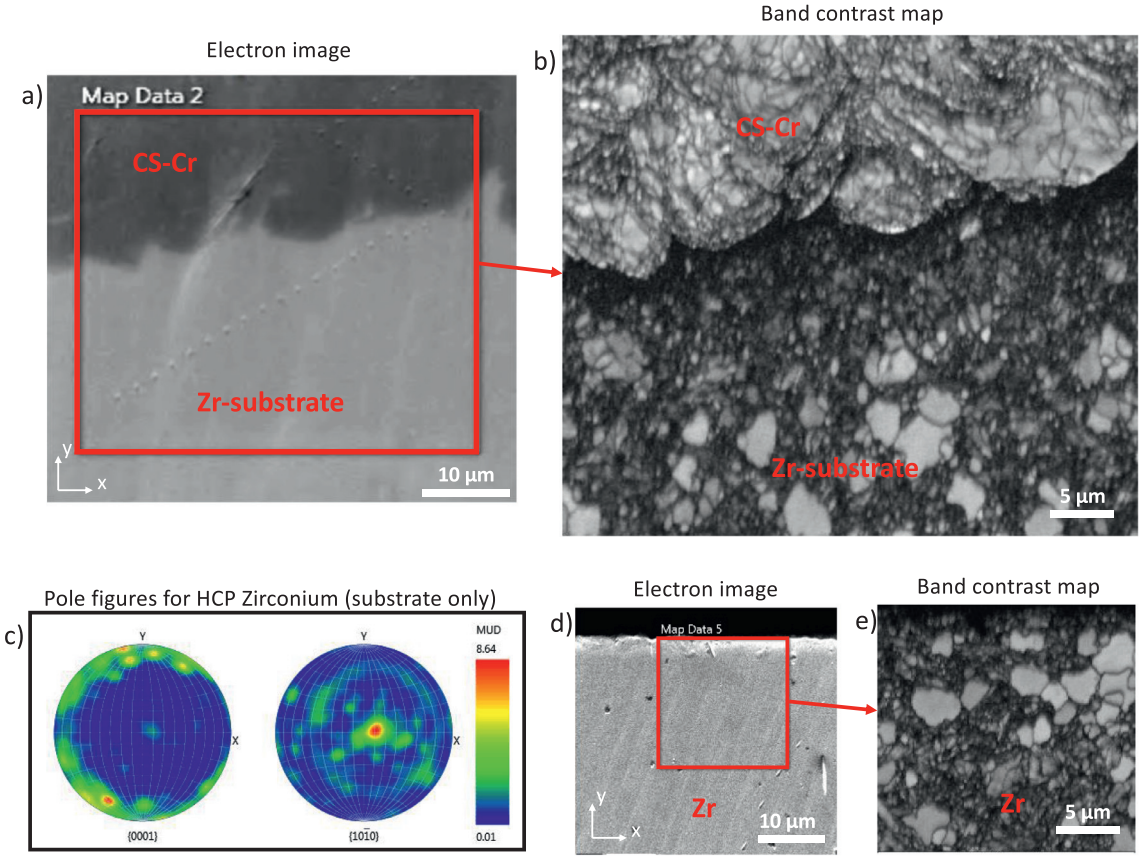

Fig. 3. EBSD mapping of cold spray Cr-coated OPZ-cladding: a) Electron image of the mapped area, b) EBSD band contrast map, c) Pole figures for {0001} and {10$\bar{1}$0} plane families in the OPZ substrate. EBSD mapping of uncoated OPZ-cladding: d) Electron image and e) EBSD band contrast map.

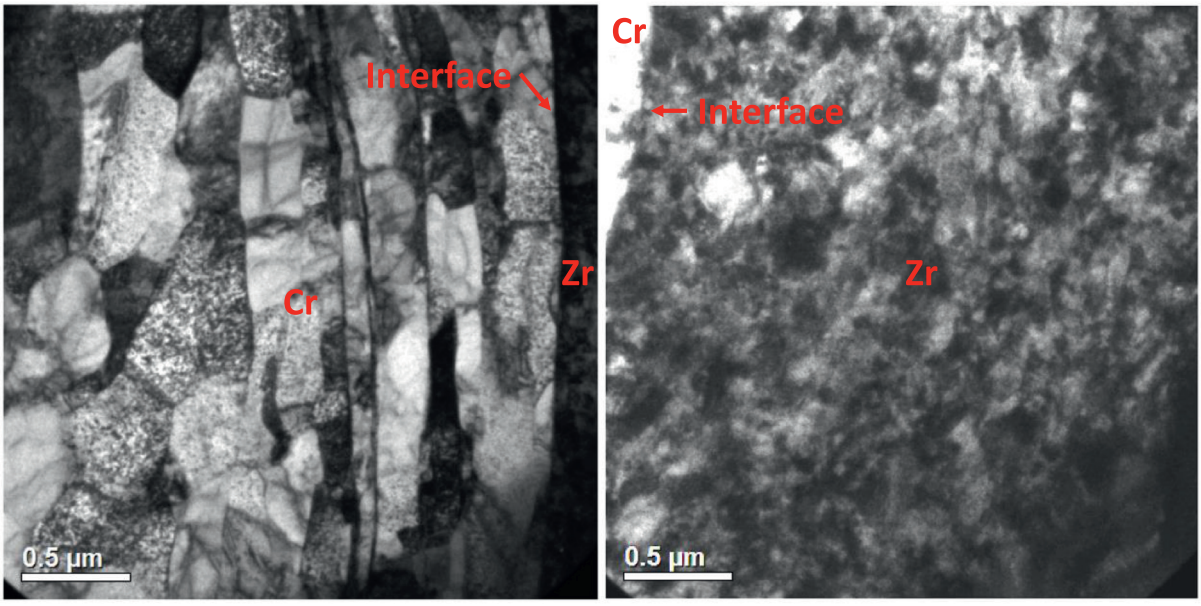

Fig. 4. BF-TEM images of CS Cr-coating/Optimized ZIRLO™ interface: Cr-side (a) and Zr-side (b).

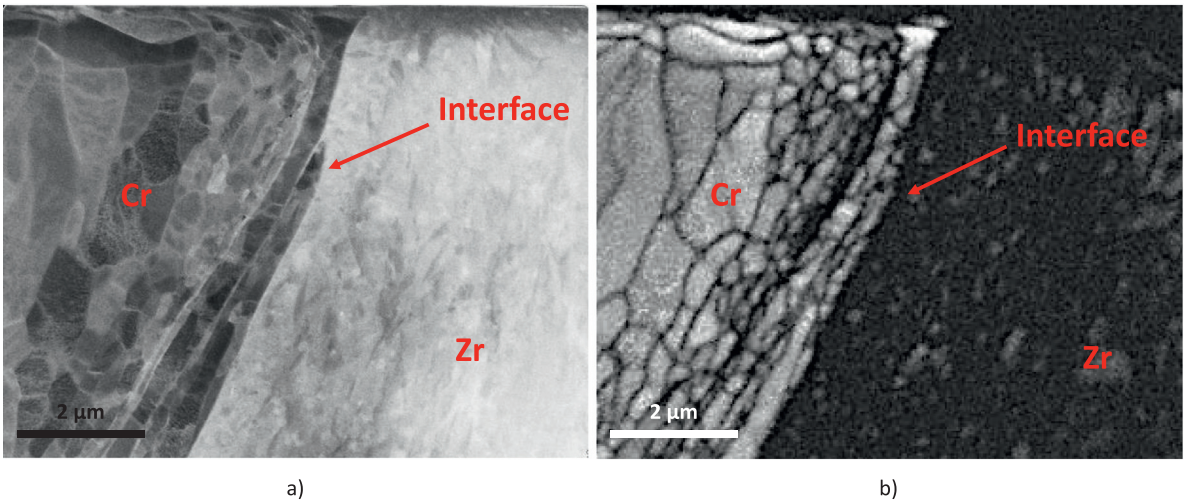

Fig. 5. STEM image (a) and TKD band contrast map (b) of CS Cr-coating/Optimized ZIRLO™ interface.

noticed in most of the grains. The Zr-side is displayed in Fig. 4b, where it is possible to see the nanocrystalline region at higher magnification, of which the SEM images offer a larger field-of-view upon (see Fig. 1). To confirm the interpretation of the contrast in the BF-TEM images, STEM imaging and TKD analysis of the same sample were conducted. The resulting STEM image and band-contrast map are contained in Fig. 5a and Fig. 5b, respectively. The TKD band contrast map defines quite clearly the grain structure of the Cr-side, in which the Cr grains appear deformed and elongated. Additionally, the size of the grains progressively increases moving away from the interface. In what appears to be the bulk of the deposited particles the grains are much larger than at the interface with the OPZ. On the Zr-side the indexing was substantially lower and less information is provided for the substrate. In any case, a few grains are visible and they seem to follow a similar trend: smaller grains close to the interface with the coating and grains gradually larger further away from the interface. In this sample, the layer of highly deformed, nanocrystalline Zr-substrate appears to be at least 2 µm thick. Due to the turbulent nature of the deposition process, it is reasonable to think that this nanocrystalline layer might be thicker or thinner depending on where on the CS-Cr/OPZ interface it is measured.

3.3. Interface chemistry

Atom probe analyses were performed with the objective of studying the chemical nature of the interface region between the Cr coating and the OPZ substrate and an example of a 3D reconstruction from such an area of interest is shown in Fig. 6. In Fig. 6a the collected Cr atoms (pink) are presented. It can be noted that three different regions are present: high, medium and low concentration of Cr atoms representing, respectively, a portion of the Cr-coating, a layer with mixed composition and the substrate with few or no Cr atoms in it. The same can be noticed in Fig. 6b regarding the Zr atoms (in blue). The interface between the Cr coating and the OPZ substrate, represented in these two images, is characterized by the presence of a volume where Cr and Zr are mixed together producing an intermixed bonding re-

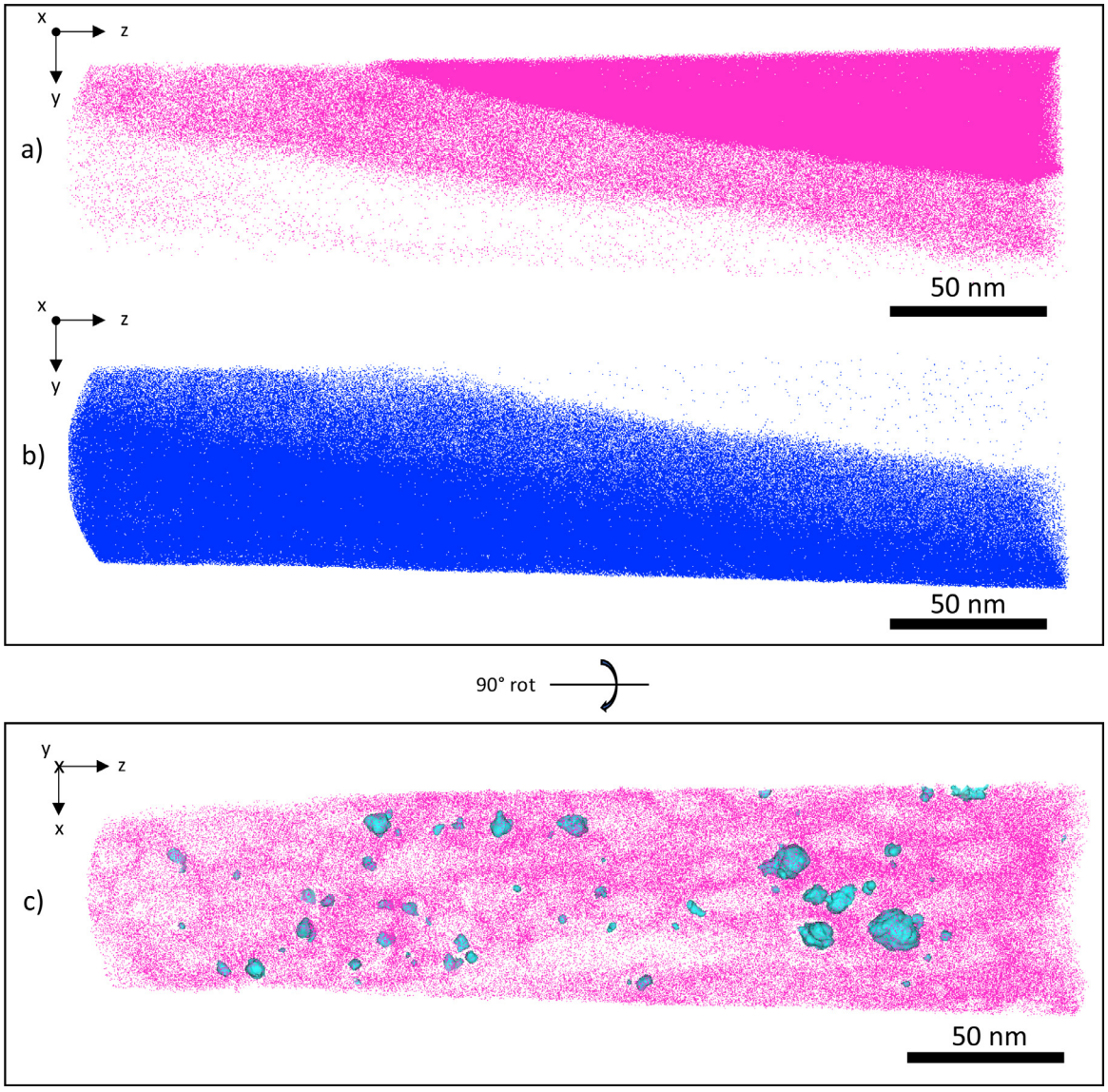

Fig. 6. 3D reconstruction of APT data from the CS Cr-coating/Optimized ZIRLO™ interface and the area around. In (a) the distribution of Cr atoms (pink, 30% of ions are shown) is displayed, in (b) the distribution of Zr atoms (Blue, 30% of ions are shown) can be seen. An image of a 15 nm slice containing the intermixed bonding region (rotated 90°) is presented, here the Cr atoms are in pink and the light-blue particles (isosurfaces at 4 at.% C) represent high concentration of C.

gion (IBR) between the two elements. In this reconstruction the intermixed layer (parallel to the y-direction) appears to be around 20 nm thick, but multiple APT measurements of the interface have demonstrated that the thickness of this region can vary from a few nanometres up to a few tens of nanometres. The portion of the reconstruction containing the IBR is extracted and rotated to better visualise features in it (see Fig. 6c). The Cr atoms (pink) present in the layer are unevenly distributed, volumes of high and low density of Cr atoms become visible in this perspective. Beside the Cr-rich regions, areas of high oxygen concentration and some small carbides are also found. Fig. 6c shows isoconcentration surfaces (isosurfaces) produced at concentration of 4 at.% carbon (plotted in light-blue). From these isosurfaces it is possible to see the distribution and sizes of such carbides.

To go beyond visual evaluation of the reconstruction, a concentration profile through the reaction layer is presented in Fig. 7a and 7b (plots obtained as 1D concentration profiles along the axis of a cylindric region of interest (ROI) with 50 nm diameter, 2 nm step size). In Fig. 7a, concentration profiles of Cr, Zr and O are shown. It is important to notice that the slopes of concentration in the proximity of the Cr-rich and the Zr-rich sides differ quite substantially, the Cr/IBR interface appears to be sharper than the Zr/IBR interface. Oxygen can be found almost exclusively in the IBR, where it reaches concentrations of around 7 at.%, it is not detected in the coating and slightly less than 1 at.% of O is found in the substrate. The behaviour of the main alloying elements of OPZ plus C is reported in Fig. 7b. Fe, Sn and Nb can all be found both in the IBR and in the substrate but not inside the Cr coating itself. Niobium seems to have been depleted from the IBR, while Fe and Sn can be found in slightly higher amounts in the mixed region than in the OPZ substrate. The higher concentration of Fe in the IBR could be explained by the dissolution of SPPs, while Sn could have diffused to the IBR during its formation. Carbon, originating probably from impurities on the former surface of the coating, is measured only inside the IBR where its concentration peaks at around 0.8 at.%. The proximity histogram (proxigram) [37] shown in Fig. 7c is calculated in 1D for the elements with respect to the carbide isosurfaces displayed in Fig. 6c. From this graph it is possible to determine the nature and composition of these carbides. Most of the carbon found in the IBR is concentrated in these carbides, which

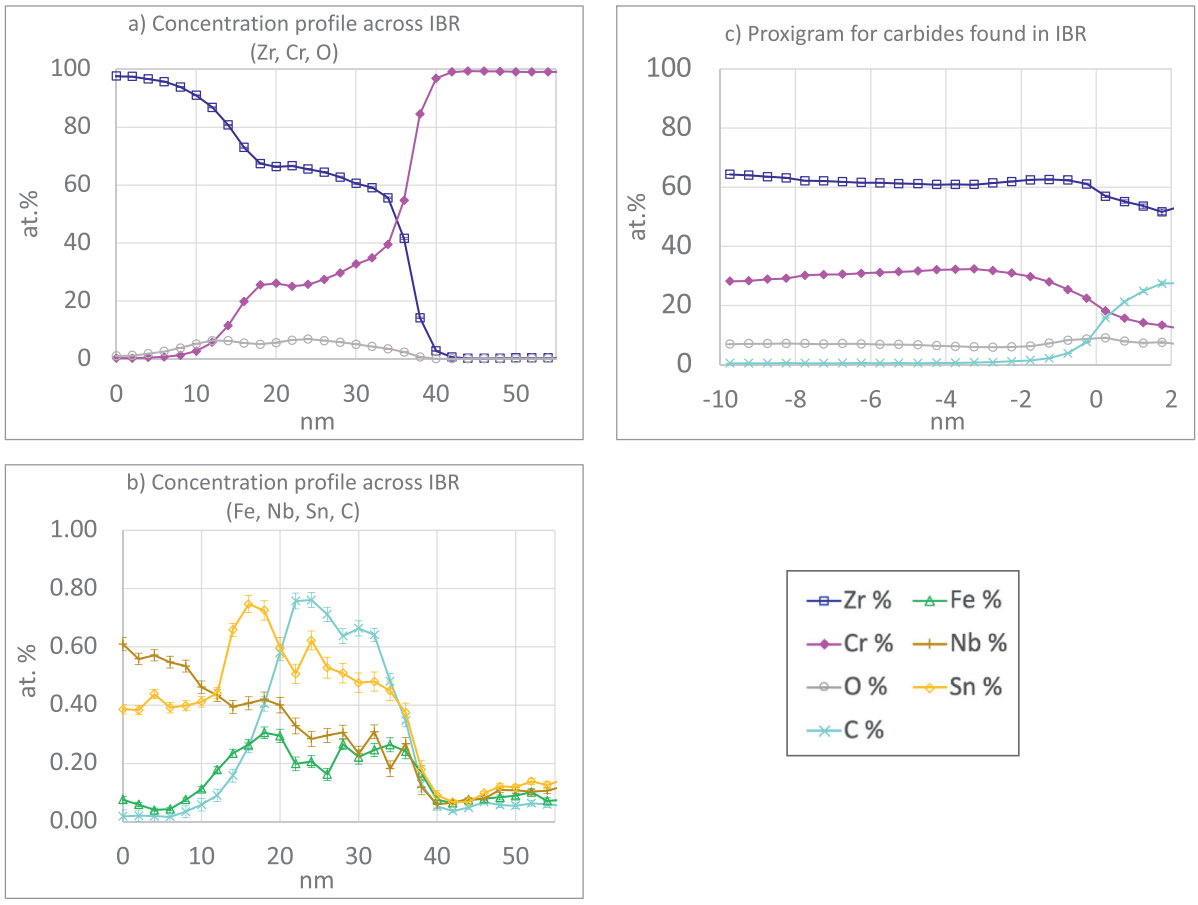

Fig. 7. (a). and (b) Concentration profiles across the intermixed bonding region found at the CS Cr-coating/Optimized ZIRLO™ interface. (c) Proxigram for carbides found embedded in the intermixed bonding region.

are mostly zirconium carbides with some substantial contents of Cr and O.

In the OPZ substrate, segregation and accumulation of elements along interfaces were frequently found. Fig. 8 contains three different reconstructions obtained, respectively, at the interface, at 100–200 nm and at 1–2 μm from the interface. For each dataset, the distribution of Cr, Fe and Nb is displayed separately. The first thing to notice is that Cr in the OPZ substrate can be found only very close to the interface and a few hundred nanometres away from it. There is no Cr detected at 1–2 μm from the coating. Moreover, most of the Cr found in the OPZ is segregated at interfaces that can be identified as sub-grain boundaries, grain boundaries or phase boundaries. Fe appears often to be coupled with Cr along the same interfaces but it can be found also 1–2 μm away from the interface. Nb can be found in SPPs, at grain boundaries and dissolved in the matrix: adjacent to the interface, Nb it is segregated along with Cr and Fe; further away it is almost totally concentrated in β-Nb SPP; and at 2 μm from the coating Nb is evenly distributed in the OPZ matrix.

Detailed concentration profiles for the aforementioned segregations are plotted in Fig. 9. In the case of the sample adjacent to the interface the trend for Cr, Fe and Nb across the more prominent accumulation of alloying elements is shown in Fig. 9a. From this graph it is clear that Cr, Fe and Nb are accumulating quite substantially. The width of the enriched region is about 20 nm which excludes the hypothesis of it being a grain boundary. The Fe content in the selected volume reaches 8 at.%, Nb rises above 4 at.% and Cr peaks at around 2 at.%. The presence of Cr can be explained by diffusion from the coating into the substrate during deposition. The high amount of Fe and Nb in such a wide region suggests the dissolution of an SPP due to localized heat and shear. In the reconstruction of the sample at 100–200 nm from the interface, two enriched areas can be found (see Fig. 9b and Fig. 9c). In this case the segregation is lower and the width of it is around 5 nm, which considering possible local magnification effects makes it likely to be grain boundaries. Cr can be found at both grain boundaries with maximum values respectively of 0.70 and 1.25 at.% (Cr Gibbs interfacial excess (Γ_{Cr}) [38] of 0.69 $\frac{atoms}{nm^2}$ and 0.75 $\frac{atoms}{nm^2}$). These are smaller concentrations if compared with the previous case: being further away from the interface it is reasonable to assume that less Cr has managed to diffuse there. Additionally, the grain boundary plotted in Fig. 9c has also a small amount of Fe segregated together with the Cr, and the Fe top concentration is 0.30 at.% (Γ_{Fe} of 0.19 $\frac{atoms}{nm^2}$). In contrast, when measuring the composition profiles for grain boundaries at 1–2 μm distance from the interface, no Cr could be found, as shown in Fig. 9d. At this distance though, it is possible to find Fe segregating at the grain boundary, as normally expected in OPZ alloys, [39,40]. In Fig. 9d Fe enrichment amounts to 0.40 at% corresponding to Γ_{Fe} of 0.58 $\frac{atoms}{nm^2}$.

3.4. Crystal structure of the interfacial region

HRTEM was used to image the interfacial region and study the crystalline structure of the IBR complementary to the APT results. In Fig. 10, HRTEM images of the interface are presented. Here, it is possible to notice the presence of lattice fringes over the entire image. The diffraction patterns obtained through fast Fourier transforms (FFTs) from the Cr and Zr regions correspond to an HCP-

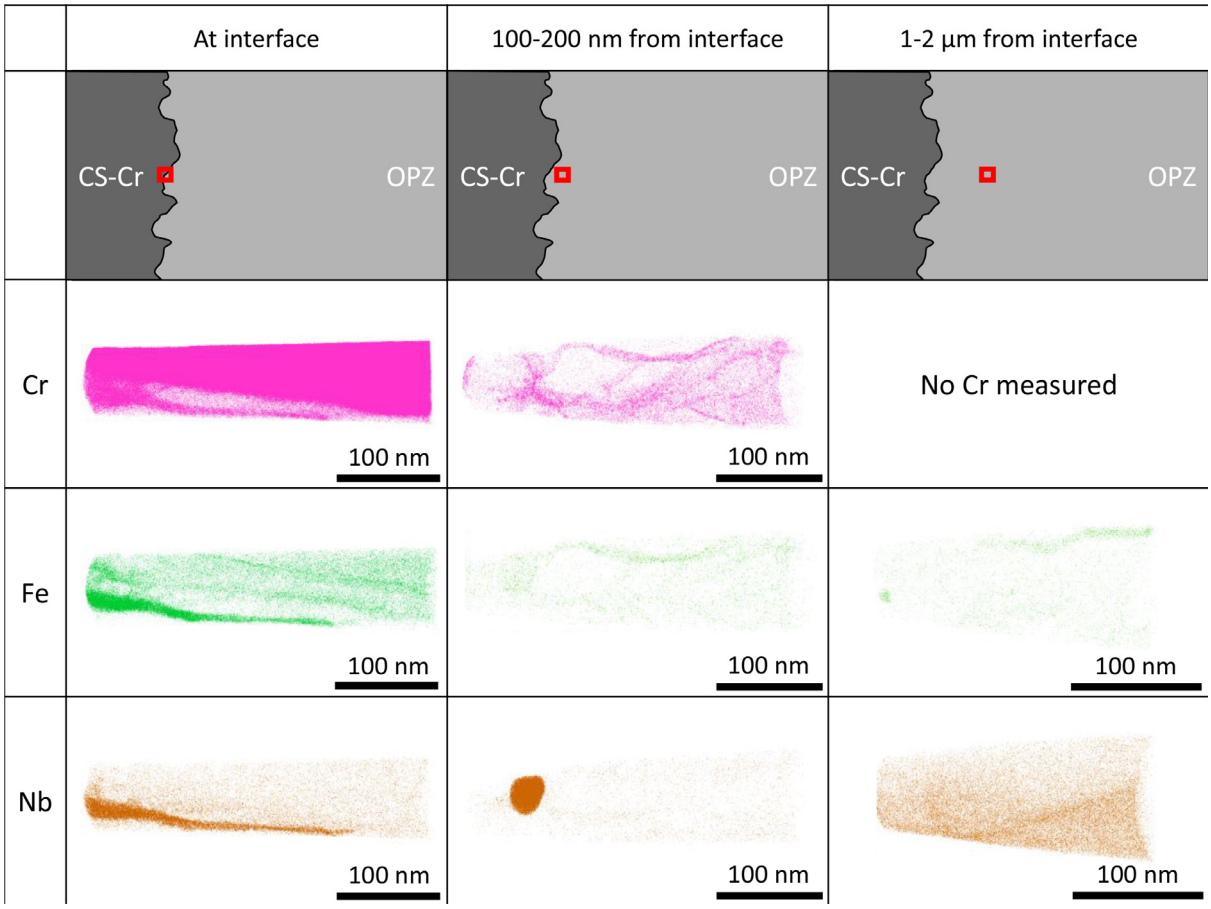

Fig. 8. 3D reconstruction of the elemental distribution of Cr, Fe and Nb in atom probe samples extracted respectively from the area around the CS Cr-coating/Optimized ZIRLO™ interface, 100–200 nm away from the interface, and 1–2 µm into the OPZ substrate.

Zr and a BCC–Cr crystalline structure, respectively, confirming that the image was taken at the interface between the coating and the substrate. The presence of lattice fringes and the associated diffraction pattern obtained from the interfacial region allow to affirm that the IBR is crystalline and not amorphous, as it has sometimes been reported for other CS coating/substrate systems [41,42]. This bonding region is indexed as an HCP-Zr structure with some distortion, most likely due to a significant supersaturation of Cr in the Zr lattice. It is relevant to highlight that in the IBR the lattice fringes are well defined only over small areas, while for the Cr and Zr regions the same orientation is maintained over large portions of the image. Across Fig. 10a-b the IBR varies in thickness between 3 nm and 16 nm, in accordance with the APT results where a similar degree of variation in thickness was observed between reconstructions. As the thickness varies, the morphology might change too and there could also be regions where the bonding layer is not crystalline or has a different crystalline structure.

4. Discussion

4.1. CS Cr-coating/Optimized ZIRLO™ interface

4.1.1. Mechanical interlocking

From the microscopy results, the interface appears to conform with a typical CS coating/substrate interface [14–16,43,44]. The effects of the difference in hardness and yield strength between the two materials can be seen in the way that the zirconium substrate deforms to a much higher degree. This type of deformation is expected to produce dynamic recrystallization that leaves a small grain size and a high concentration of dislocations in both materials [14,27,45]. In fact, SEM, EBSD, TKD and BF-TEM analysis outlined such a microstructure: nanocrystalline regions and highly deformed grains at the microscale; morphologically rough CS-Cr/OPZ interface with bulges of Cr metal wrapped by the OPZ substrate at a larger scale. The formation of a thin layer of intermixed composition was observed. This indicates that locally the temperature must have been quite high, since the formation of a Cr-Zr intermetallic compound was reported to form only in material exposed to high temperatures [7]. The formation of a brittle intermetallic compound at the interface between coating and substrate is usually considered extremely harming to the coating adhesion. It can result in delamination or spallation of the coating associated with exposure of the substrate and loss of corrosion protection. In the studied case, though, the geometry of the interface produces a mechanical interlocking that can prevent any macroscopic stress to directly load the presumably brittle interface. As a result, the interface is exposed to a mixture of compressive and tensile stresses unable to cause actual spallation. The effectiveness of this structure is confirmed by the wide range of corrosion and mechanical tests performed on CS Cr-coated OPZ claddings with no delamination of the coating reported [7,10,29]. The mentioned mechanical interlocking is therefore to be considered a strong advantage provided by the CS deposition method that guarantees strong adhesion between the coating and the substrate.

4.1.2. Metallurgical bonding: the intermixed bonding region

The APT results highlighted the presence of an IBR at the interface between coating and substrate. This IBR was found to be

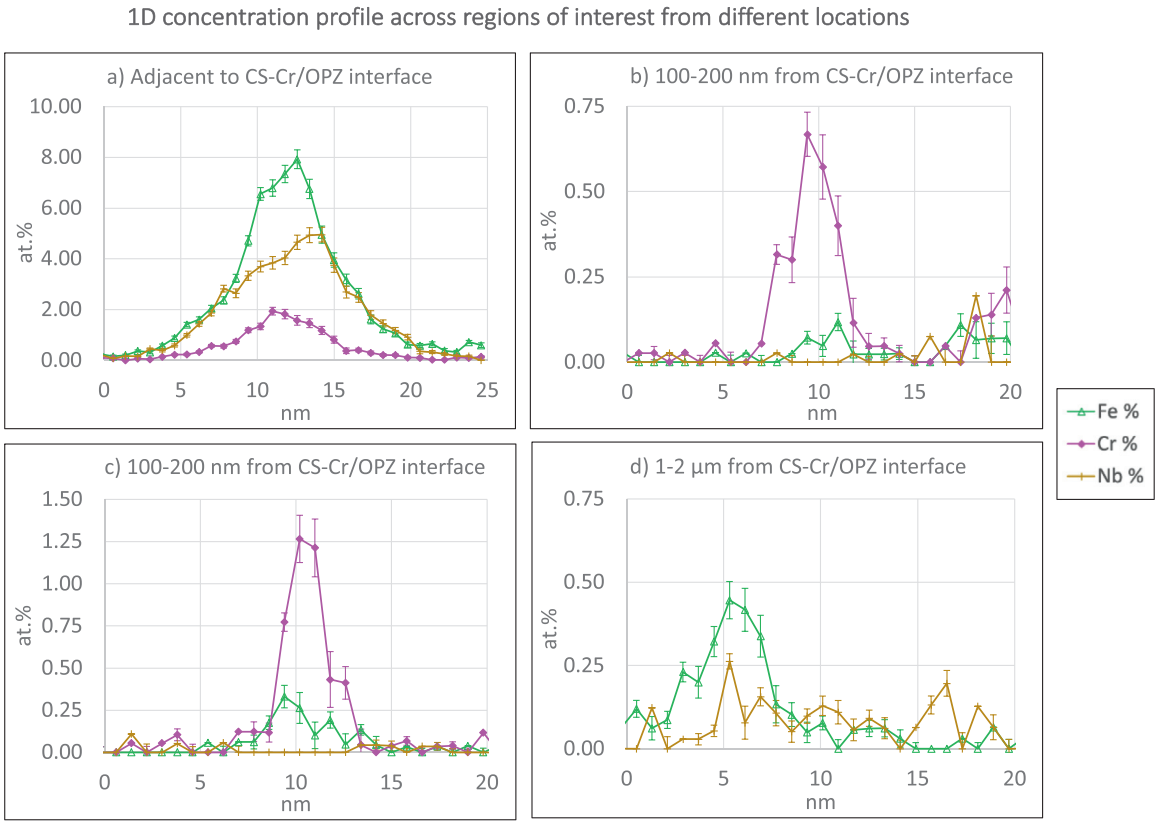

Fig. 9. Concentration profiles for Fe, Nb and Cr at different locations: (a) Concentration profile across dissolved SPP adjacent to the CS Cr-coating/Optimized ZIRLO™ interface; (b) and (c) concentration profiles across Cr-enriched and Fe/Cr-enriched grain boundaries few hundreds of nanometres away from the interface, (d) concentration profiles through Fe-enriched grain boundaries 1–2 µm into the OPZ bulk.

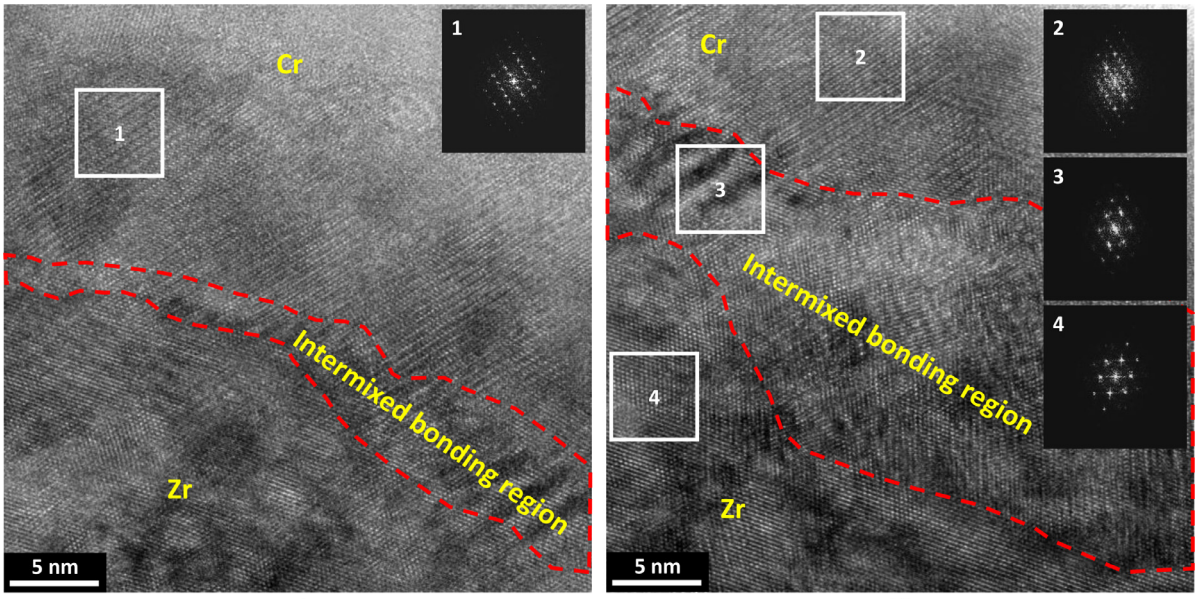

Fig. 10. HRTEM of two regions of the CS Cr-coating/Optimized ZIRLO™ interface: Cr-side at the top, Zr-substrate at the bottom of the images, intermixed bonding region (highlighted with a red dashed line) cuts across the centre of the image left to right.

present in all analyses with the same general features; hence, it can be considered a characteristic of the studied system. This mixed region has a thickness that varies between a few nanometres up to a few tens of nanometres; and a composition of about 60–70 at.% Zr, 30–40 at.% Cr, with up to 8–10 at.% O and 0.80 at.% C (see Figs. 6-7). Fe, Sn and Nb (all alloying elements used in OPZ [46]) can be found in this layer as well. Overall, the composition of the region suggests that this layer has been produce by a highly localised shearing and heating of a small volume of the OPZ substrate and the Cr-particles. This process, referred to as adiabatic shear instability mechanism for particle/substrate bonding, is often deemed responsible for the formation of the strong metallur-

gical bonding typical for cold spray deposition [17,47–49], and it could be the cause behind the formation of the measured IBR. In particular, the localized heat spike could have promoted significant bulk diffusion of Cr into the Zr-substrate, explaining the high content of Cr measured in the IBR. The oxygen content (8–10 at.%) is more difficult to explain. The dissolution of the native oxide scale into the IBR seems unlikely due to the extremely short duration of a particle collision, and it is too low to be attributed to the direct presence of ZrO_2. This amount of oxygen seems to be closer to the typical composition of the Zr metal laying underneath the ZrO_2 scale, this region is called oxygen diffusion zone (or Zr(O)), it forms during Zr oxidation [50] and it is normally found ahead of the oxide front. The amount of O in it can vary from 1 at.% (O content in Zr-alloys) up to around 30 at.% where saturation is reached [51,52]. The studied material was as-fabricated, the oxide formed on Zr in air at room temperature is usually extremely thin, in the order of 5–20 nm [53], followed by a thin oxygen diffusion zone. The IBR composition seems to line up with that of an oxygen diffusion zone, but this would require an explanation for the disappearance of the native oxide scale. The oxide scale evolution during cold spray deposition is well documented in literature for other coating/substrate systems [54–56] and could explain why the native oxide is not found at the coating/substrate interface and why 8–10 at.% O is found in the IBR. During deposition, part of the native oxide is lost due to the high velocity impact, the remaining part is still present at the coating/substrate interface but it has been cracked into small segments and pulled apart to accommodate the plastic deformation of the metal. The result is small segments of oxide that are sparse and far between. This process uncovers the Zr substrate underneath exposing the oxygen diffusion zone which ends up forming the IBR. The carbon could be explained as residue of grease or some other contaminant present on the cladding surface before the deposition of the coating. Zirconium has lower hardness than chromium, when impacted by a Cr-particle, Zr is subjected to a higher degree of plastic deformation. This can be clearly appreciated from the SEM images in Fig. 1 and from the EBSD maps in Fig. 3. The heat locally produced during adiabatic shear is strictly correlated to the amount of plastic flow [25,57], thus it is reasonable to expect more heat generated in the substrate with Zr being the most affected by the adiabatic shear instability phenomenon. Another proof of the heat spike behind the formation of the IBR is the presence of carbon, found mostly in the form of zirconium carbides. As shown by Fig. 7c, outside the carbides, the concentration of carbon in the IBR is essentially zero. All the carbon seems to be contained in these zirconium carbide particles that cannot form at room temperature. The exposure to elevated temperatures, even if only for a short time, could explain how these nanometre-sized Zr-carbides have formed. The C concentration inside the measured carbides approaches 30 at.%, but the thermodynamically allowed composition range for ZrC is 33–49.6 at.% [58]; additionally, Zr concentration peaks in the proximity of the carbide/IBR interface as if Zr was diffusing out of the carbides in an attempt by the system to reach equilibrium before being frozen in a metastable state. The IBR had a distorted HCP-Zr crystalline structure, as obtained from the HRTEM data (Fig. 10), which would sustain the hypothesis of the adiabatic shear instability affecting almost exclusively Zr. As can be seen in Fig. 6c, the IBR is characterised by the presence of regions of higher and lower concentration of Cr. This inhomogeneity of the layer could both be interpreted as incomplete mixing or as an attempt by the system to separate into more thermodynamically stable phases. Since the carbides had time to form depleting almost all carbon from the IBR matrix, there must have been enough time for some diffusion to occur also for Cr and Zr. This suggests that the fluctuations in the Cr content should be interpreted as the initial stage of a phase separation, but because Zr and Cr diffuse much slower than carbon they would have required more time to reach equilibrium. The thickness of the IBR was found to vary depending on where on the CS-Cr/OPZ interface it was measured. This is caused by the chaotic nature of the CS deposition method on the microscopic scale: most of the energy of the impact is transmitted to the substrate in proximity of the forefront of the incoming particle, while other regions experience less intense shear stresses [43,45]. As a consequence, the IBR formed at the initial point of contact with the particle will have been exposed to different conditions from the IBR formed at the periphery of the impact. It is relevant to underline that due to the rapid cooling, the phases that form the IBR are not in thermodynamic equilibrium [59]. Looking at a Cr-Zr phase diagram [60] it is easy to see that the overall composition measured for the layer (Zr 60–70 at.% and Cr 30–40 at.%) falls into a field where α-Zr and ZrCr2 co-exist. If kinetically allowed by a sufficiently high temperature, the IBR is expected to evolve forming both phases. Moreover, the presence of the IBR at the interface might facilitate the formation of new phases by reducing substantially the energy needed for nucleation. CS Cr-coatings on OPZ cladding were reported to form the ZrCr2 intermetallic compound when exposed to temperatures above 1130 °C (for 10 min) [7] and the same phenomenon was reported on Zr-Cr diffusion couples for a temperature as low as 750 °C when exposed for longer times [30]. In these studies, the formation of the intermetallic compound did not result in spallation of the coating but it is still important to keep in consideration that the presence of this IBR could have an effect on phase nucleation and growth, particularly at elevated temperature or under irradiation.

4.2. Effects on the substrate microstructure

4.2.1. Heat affected zone and the chemistry of grain boundaries

Small amounts of Cr were measured in the OPZ substrate, and this finding was restricted to the substrate region immediately close to the coating interface. Chromium is not amongst the alloying elements used in OPZ [46], which implies that the measured Cr must have diffused from the coating into the Zr. Besides, the range of this diffusion is limited, and no Cr was found in the APT reconstruction of a sample lifted-out at 1–2 μm distance from the CS-Cr/OPZ interface, as can be seen in Fig. 8. It is possible to assume that the same heat spike that allowed the formation of the IBR could have produced the conditions for grain boundary diffusion of Cr to occur. Diffusivity along grain boundaries is usually 2–5 order of magnitude higher than bulk-diffusivity [61–63], and considering the high density of grain boundaries found in the nanocrystalline layer, it is possible to imagine Cr atoms penetrating into the Zr-substrate along the network of grain boundaries to distances of few hundreds of nanometres. Interestingly, no Zr was found in the Cr coating. The reported diffusion coefficient of Cr into Zr is many orders of magnitude higher than the diffusion coefficient of Zr into Cr or Zr self-diffusion [30,64–67]. It is therefore reasonable to find Cr diffusing into the OPZ substrate without any measurable amount of Zr diffusing into the coating. This can be interpreted as a thin heat affected zone (HAZ) located in the substrate immediately adjacent to the IBR. The thickness of the HAZ seems to be less than 1–2 μm, probably not making it detrimental for the overall cladding performance. Another marker that can be used to estimate the extent of the HAZ is the distribution of SPPs in the substrate. As it is displayed in Fig. 1b, SPPs can be found evenly distributed over the cross-section. The only hint to the presence of a HAZ is a thin layer depleted of SPPs. This layer close to the interface appears to be thinner than 0.5 μm in this image. Moving to the APT data in Fig. 8, what looks like a dissolved SPP can be found at 50 nm distance from the interface, while at 100–200 nm from the interface an unaltered β-Nb SPP is detected. In conclusion, the HAZ seems to extend for a few hundreds of nanometres

from the interface, SPPs are dissolved in the first 100 nm and Cr penetrates along grain boundaries into the Zr-substrate for at least 100–200 nm.

4.2.2. Nano-crystalline layer

A highly deformed nanocrystalline layer can be identified already from the SEM images. Here, it is possible to see the high degree of deformation that characterizes both materials, in particular the OPZ. Further confirmation of the presence of this layer is obtained from the EBSD, BF-TEM and TKD data presented in Figs. 3, 4 and 5, respectively. In the EBSD map in particular, this layer appears as a 1–4 μm thick dark band in the OPZ substrate just below the CS-Cr/OPZ interface. The same region is analysed in further detail at higher magnification in the TKD map where some of the nano-sized grains start to become more defined and visible. The volume of material in question has undergone a high degree of plastic deformation. The plastic flow has induced the generation of a large amount of dislocations, which beyond a certain concentration start to organize and align forming sub-grain boundaries and consequently new grain boundaries. This process of in-situ grain refinement via dynamic recrystallization is a direct consequence of the CS deposition method and it is well documented for many coating/substrate systems obtained through the use of this technique [45,68]. It is difficult to obtain clear Kikuchi bands from this layer, which is highly deformed and nano-sized. This explains the low band contrast and the dark colour that identifies this region in TKD and EBSD maps. Nevertheless, it is possible to see that the size of the grains that form the layer starts far below 1 μm (probably down to 100 nm in size) close to the CS-Cr/OPZ interface and gradually becomes larger while moving into the bulk of the substrate. Beyond the edge of the dark band, the grains begin to grow in size larger than 1 μm, but the effects of the coating deposition on the substrate microstructure extend up to 10–15 μm from the CS-Cr/OPZ interface. Only at this distance the alternating of large and fine grains that characterizes the microstructure of a partially recrystallized OPZ cladding starts to come back (see Figs. 3b and 3e). Since the cladding wall is around 900 μm thick, this effect does not influence the overall mechanical properties of the cladding. Besides, diffusion is enhanced in nanocrystalline materials due to the high density of lattice defects and grain boundaries. As a consequence, the presence of the reported nanocrystalline layer could potentially modify the local behaviour of the OPZ alloy, particularly in respect of diffusive processes such as corrosion [69]. Additionally, nanocrystalline materials can be prone to recrystallization at relatively low temperatures [70]. This suggests that it could be possible for this nanocrystalline layer to undergo recrystallization even at reactor operating temperatures.

5. Conclusions

The microstructure of an as-fabricated CS Cr-coating deposited on an OPZ alloy cladding is studied with particular focus on the interfacial region between the coating and the substrate. The coating appeared to be highly plastically deformed and mechanical interlocking could be observed between the coating and the substrate, as expected for a component produced with CS technology. A 10–20 nm thick, crystalline, IBR was discovered at the CS-Cr/OPZ interface. This layer is thought to have formed during the CS deposition process as a consequence of localized shearing and heating of the outermost surface of the cladding resulting in the bulk diffusion of Cr from the adjacent Cr-coating into the Zr-substrate, as suggested by its chemical composition. A secondary effect caused by this localized temperature spike is the presence of a HAZ that extends a few hundred nanometres into the substrate. The HAZ is outlined by the presence of Cr into the substrate at grain boundaries. At a larger scale, the intense shear stresses and plastic deformation at which the periphery of sprayed particles and the substrate surface are exposed during deposition have produced a nano-crystalline layer. The nano-crystalline layer is characterized by grains ranging in size from below 100 nm (adjacent to the interface) up to almost 1 μm (at 10 μm distance from the interface) before the reestablishment of the unaffected microstructure of the bulk. Overall, the metallurgical bonding and the mechanical interlocking guarantee a very good adhesion of the coating while the nano-crystalline volume is reckoned too thin to have any significant effect on the mechanical properties of the cladding. However, it is relevant to take the following effects into consideration; i) the presence of the observed IBR can greatly reduce the energy barrier for the nucleation of new phases at the CS-Cr/OPZ interface, ii) the increased density of grain boundaries in the nano-crystalline region could facilitate unwanted diffusion processes, iii) the nano-crystalline layer could undergo recrystallization at relatively low temperatures.

Declaration of Competing Interest

The authors declare that they have no known competing financial interests or personal relationships that could have appeared to influence the work reported in this paper.

CRediT authorship contribution statement

Andrea Fazi: Investigation, Writing – original draft, Visualization, Conceptualization. **Hisham Aboulfadl:** Methodology, Writing – review & editing. **Anand H.S. Iyer:** Methodology. **Mohammad Sattari:** Methodology. **Krystyna Marta Stiller:** Writing – review & editing, Conceptualization. **Pratik Lokhande:** Methodology. **Mattias Thuvander:** Supervision, Project administration, Funding acquisition, Writing – review & editing, Conceptualization. **Hans-Olof Andren:** Writing – review & editing, Conceptualization.

Acknowledgments

This project is financially supported by the Swedish Foundation for Strategic Research (SSF). (Grant number: EM16-0031)

Westinghouse Electric SE are acknowledged for providing the analysed material.

All the experimental work presented in this paper was performed at Chalmers Materials Analysis Laboratory (CMAL).

References

[1] S.J. Zinkle, K.A. Terrani, J.C. Gehin, L.J. Ott, L.L. Snead, Accident tolerant fuels for LWRs: a perspective, J. Nucl. Mater. 448 (2014) 374–379, doi:10.1016/j.jnucmat.2013.12.005.

[2] K.A. Terrani, Accident tolerant fuel cladding development: promise, status, and challenges, J. Nucl. Mater. 501 (2018) 13–30, doi:10.1016/j.jnucmat.2017.12.043.

[3] R.B. Rebak, Worldwide development of accident tolerant fuels, areas of study, claddings, and fuels, in: Accid. Toler. Mater. Light Water React. Fuels, Elsevier, 2020, pp. 43–62, doi:10.1016/b978-0-12-817503-3.00003-1.

[4] C. Tang, M. Stueber, H.J. Seifert, M. Steinbrueck, Protective coatings on zirconium-based alloys as accident-tolerant fuel (ATF) claddings, Corros. Rev. 35 (2017) 141–165, doi:10.1515/corrrev-2017-0010.

[5] J.C. Brachet, M.Le Saux, M.Le Flem, S. Urvoy, E. Rouesne, T. Guilbert, C. Cobac, F. Lahogue, J. Rousselot, M. Tupin, P. Billaud, C. Hossepied, F. Schuster, F. Lomello, A. Billard, G. Velisa, E. Monsifrot, J. Bischoff, A. Ambard, On-Going Studies At Cea On Chromium Coated Zirconium Based Nuclear Fuel Claddings For Enhanced Accident Tolerant Lwrs Fuel, TopFuel (2015) 31–38.

[6] J. Bischoff, C. Delafoy, C. Vauglin, P. Barberis, C. Roubeyrie, D. Perche, D. Duthoo, F. Schuster, J.C. Brachet, E.W. Schweitzer, K. Nimishakavi, AREVA NP's enhanced accident-tolerant fuel developments: focus on Cr-coated M5 cladding, Nucl. Eng. Technol. 50 (2018) 223–228, doi:10.1016/j.net.2017.12.004.

[7] H. Yeom, B. Maier, G. Johnson, T. Dabney, M. Lenling, K. Sridharan, High temperature oxidation and microstructural evolution of cold spray chromium coatings on Zircaloy-4 in steam environments, J. Nucl. Mater. 526 (2019) 151737, doi:10.1016/j.jnucmat.2019.151737.

[8] J. Bischoff, C. Delafoy, N. Chaari, C. Vauglin, K. Buchanan, P. Barberis, E. Monsifrot, J.-C.B.F. Schuster, K. Nimishakavi, Cr coated cladding Development At Framatome, TopFuel (2018) 1–7.

[9] J.C. Brachet, E. Rouesne, J. Ribis, T. Guilbert, S. Urvoy, G. Nony, C. Toffolon-Masclet, M.Le Saux, N. Chaabane, H. Palancher, A. David, J. Bischoff, J. Augereau, E. Pouillier, High temperature steam oxidation of chromium-coated zirconium-based alloys: kinetics and process, Corros. Sci 167 (2020) 108537, doi:10.1016/j.corsci.2020.108537.

[10] B. Maier, H. Yeom, G. Johnson, T. Dabney, J. Walters, P. Xu, J. Romero, H. Shah, K. Sridharan, Development of cold spray chromium coatings for improved accident tolerant zirconium-alloy cladding, J. Nucl. Mater. 519 (2019) 247–254, doi:10.1016/j.jnucmat.2019.03.039.

[11] R.V. Umretiya, B. Elward, D. Lee, M. Anderson, R.B. Rebak, J.V. Rojas, Mechanical and chemical properties of PVD and cold spray Cr-coatings on Zircaloy-4, J. Nucl. Mater. 541 (2020) 152420, doi:10.1016/j.jnucmat.2020.152420.

[12] D.L. Gilmore, R.C. Dykhuizen, R.A. Neiser, T.J. Roemer, M.F. Smith, Particle velocity and deposition efficiency in the cold spray process, J. Therm. Spray Technol. 8 (1999) 576–582, doi:10.1361/105996399770350278.

[13] M.F. Smith, Comparing cold spray with thermal spray coating technologies, Cold Spray Mater. Depos. Process Fundam. Appl. 1911 (2007) 43–61, doi:10.1533/9781845693787.1.43.

[14] P. Cavaliere, Cold-Spray Coatings: Recent Trends And Future Perspectives, Springer, 2017, doi:10.1007/978-3-319-67183-3.

[15] T. Stoltenhoff, H. Kreye, H.J. Richter, An analysis of the cold spray process and its coatings, J. Therm. Spray Technol. 11 (2002) 542–550, doi:10.1361/105996302770348682.

[16] C. Lee, J. Kim, Microstructure of Kinetic Spray Coatings: a Review, J. Therm. Spray Technol. 24 (2015) 592–610, doi:10.1007/s11666-015-0223-5.

[17] H. Assadi, F. Gärtner, T. Stoltenhoff, H. Kreye, Bonding mechanism in cold gas spraying, Acta Mater 51 (2003) 4379–4394, doi:10.1016/S1359-6454(03)00274-X.

[18] S.M. Hassani-Gangaraj, A. Moridi, M. Guagliano, Critical review of corrosion protection by cold spray coatings, Surf. Eng. 31 (2015) 803–815, doi:10.1179/1743294415Y.0000000018.

[19] B. Maier, H. Yeom, G. Johnson, T. Dabney, J. Walters, J. Romero, H. Shah, P. Xu, K. Sridharan, Development of Cold Spray Coatings for Accident-Tolerant Fuel Cladding in Light Water Reactors, JOM 70 (2018) 198–202, doi:10.1007/s11837-017-2643-9.

[20] F. Gärtner, T. Stoltenhoff, T. Schmidt, H. Kreye, The cold spray process and its potential for industrial applications, J. Therm. Spray Technol. 15 (2006) 223–232, doi:10.1361/105996306X108110.

[21] E. Irissou, J.G. Legoux, A.N. Ryabinin, B. Jodoin, C. Moreau, Review on cold spray process and technology: part I - Intellectual property, J. Therm. Spray Technol. 17 (2008) 495–516, doi:10.1007/s11666-008-9203-3.

[22] S.V. Klinkov, V.F. Kosarev, M. Rein, Cold spray deposition: significance of particle impact phenomena, Aerosp. Sci. Technol. 9 (2005) 582–591, doi:10.1016/j.ast.2005.03.005.

[23] Y. Xie, S. Yin, C. Chen, M.P. Planche, H. Liao, R. Lupoi, New insights into the coating/substrate interfacial bonding mechanism in cold spray, Scr. Mater. 125 (2016) 1–4, doi:10.1016/j.scriptamat.2016.07.024.

[24] S. Guetta, M.H. Berger, F. Borit, V. Guipont, M. Jeandin, M. Boustie, Y. Ichikawa, K. Sakaguchi, K. Ogawa, Influence of particle velocity on adhesion of cold-sprayed splats, J. Therm. Spray Technol. 18 (2009) 331–342, doi:10.1007/s11666-009-9327-0.

[25] G. Bae, S. Kumar, S. Yoon, K. Kang, H. Na, H.J. Kim, C. Lee, Bonding features and associated mechanisms in kinetic sprayed titanium coatings, Acta Mater. 57 (2009) 5654–5666, doi:10.1016/j.actamat.2009.07.061.

[26] G. Bae, J. Il Jang, C. Lee, Correlation of particle impact conditions with bonding, nanocrystal formation and mechanical properties in kinetic sprayed nickel, Acta Mater. 60 (2012) 3524–3535, doi:10.1016/j.actamat.2012.03.001.

[27] E. Calla, D.G. McCartney, P.H. Shipway, Effect of deposition conditions on the properties and annealing behavior of cold-sprayed copper, J. Therm. Spray Technol. 15 (2006) 255–262, doi:10.1361/105996306X108192.

[28] K. Kang, H. Park, G. Bae, C. Lee, Microstructure and texture of Al coating during kinetic spraying and heat treatment, J. Mater. Sci. 47 (2012) 4053–4061, doi:10.1007/s10853-012-6259-8.

[29] H. Shah, J. Romero, P. Xu, B. Maier, G. Johnson, J. Walters, T. Dabney, H. Yeom, K. Sridharan, Development of Surface Coatings for Enhanced Accident Tolerant Fuel, Water React. Fuel Perform. Meet. (2017).

[30] W. Xiang, S. Ying, Reaction Diffusion In Chromium-Zircaloy-2 System (Cnic-01562), National Key Laboratory For Nuclear Fuel And Materials, Nuclear Power Institute Of China, Chengdu, China, 2001.

[31] K. Thompson, D. Lawrence, D.J. Larson, J.D. Olson, T.F. Kelly, B. Gorman, In situ site-specific specimen preparation for atom probe tomography, Ultramicroscopy 107 (2007) 131–139, doi:10.1016/j.ultramic.2006.06.008.

[32] R.M. Langford, M. Rogers, In situ lift-out: steps to improve yield and a comparison with other FIB TEM sample preparation techniques, Micron 39 (2008) 1325–1330, doi:10.1016/j.micron.2008.02.006.

[33] J.P. Foster, H.K. Yueh, R.J. Comstock, ZIRLO™ cladding improvement, ASTM Spec. Tech. Publ. (2009) 457–470, doi:10.1520/stp48149s.

[34] C.A. Volkert, A.M. Minor, Focused ion beam microscopy and micromachining, MRS Bull 32 (2007) 389–395, doi:10.1557/mrs2007.62.

[35] K.V.M. Krishna, S.K. Sahoo, I. Samajdar, S. Neogy, R. Tewari, D. Srivastava, G.K. Dey, G.H. Das, N. Saibaba, S. Banarjee, Microstructural and textural developments during Zircaloy-4 fuel tube fabrication, J. Nucl. Mater. 383 (2008) 78–85, doi:10.1016/j.jnucmat.2008.08.050.

[36] E. Tenckhoff, Review of Deformation Mechanisms, Texture, and Mechanical Anisotropy in Zirconium and Zirconium Base Alloys, J. ASTM Int. 2 (2005) 25–52.

[37] B. Gault, M.P. Moody, J.M. Cairney, S.P. Ringer, in: Atom Probe Microscopy and Materials Science, Springer New York, New York, NY, 2012, pp. 299–311, doi:10.1007/978-1-4614-3436-8_9.

[38] O.C. Hellman, D.N. Seidman, Measurement of the Gibbsian interfacial excess of solute at an interface of arbitrary geometry using three-dimensional atom probe microscopy, Mater. Sci. Eng. A. 327 (2002) 24–28, doi:10.1016/S0921-5093(01)01885-8.

[39] D. Hudson, G.D.W. Smith, Initial observation of grain boundary solute segregation in a zirconium alloy (ZIRLO) by three-dimensional atom probe, Scr. Mater. 61 (2009) 411–414, doi:10.1016/j.scriptamat.2009.04.032.

[40] B. Tao, B. Luan, R. Qiu, Q. Fang, L. Cao, Y. Liu, X. Zhang, R. Liu, Q. Liu, Analysis of atomic distribution near grain boundary in Zr–Sn–Nb–Fe-(Cu) alloys by atom probe tomography, J. Nucl. Mater. 515 (2019) 135–139, doi:10.1016/j.jnucmat.2018.12.033.

[41] X.T. Luo, C.X. Li, F.L. Shang, G.J. Yang, Y.Y. Wang, C.J. Li, High velocity impact induced microstructure evolution during deposition of cold spray coatings: a review, Surf. Coatings Technol. 254 (2014) 11–20, doi:10.1016/j.surfcoat.2014.06.006.

[42] Y. Xiong, K. Kang, G. Bae, S. Yoon, C. Lee, Dynamic amorphization and recrystallization of metals in kinetic spray process, Appl. Phys. Lett. 92 (2008), doi:10.1063/1.2928218.

[43] O. Bielousova, J. Kocimski, R.G. Maev, I. Smurov, W. Scharff, V. Leshchynsky, Localisation of deformation in cold gas dynamic spraying, Surf. Eng. 32 (2016) 655–662, doi:10.1179/1743294415Y.0000000059.

[44] Y. Zou, D. Goldbaum, J.A. Szpunar, S. Yue, Microstructure and nanohardness of cold-sprayed coatings: electron backscattered diffraction and nanoindentation studies, Scr. Mater. 62 (2010) 395–398, doi:10.1016/j.scriptamat.2009.11.034.

[45] Y. Zou, W. Qin, E. Irissou, J.G. Legoux, S. Yue, J.A. Szpunar, Dynamic recrystallization in the particle/particle interfacial region of cold-sprayed nickel coating: electron backscatter diffraction characterization, Scr. Mater. 61 (2009) 899–902, doi:10.1016/j.scriptamat.2009.07.020.

[46] G. Sabol, ZIRLO™ — An Alloy Development Success, J. ASTM Int. 2 (2005) 12942, doi:10.1520/JAI12942.

[47] M. Grujicic, C.L. Zhao, W.S. DeRosset, D. Helfritch, Adiabatic shear instability based mechanism for particles/substrate bonding in the cold-gas dynamic-spray process, Mater. Des. 25 (2004) 681–688, doi:10.1016/j.matdes.2004.03.008.

[48] M. Hassani-Gangaraj, D. Veysset, V.K. Champagne, K.A. Nelson, C.A. Schuh, Adiabatic shear instability is not necessary for adhesion in cold spray, Acta Mater. 158 (2018) 430–439, doi:10.1016/j.actamat.2018.07.065.

[49] H. Assadi, F. Gärtner, T. Klassen, H. Kreye, Comment on 'Adiabatic shear instability is not necessary for adhesion in cold spray, Scr. Mater. 162 (2019) 512–514, doi:10.1016/j.scriptamat.2018.10.036.

[50] P. Tejland, M. Thuvander, H.O. Andrén, S. Ciurea, T. Andersson, M. Dahlbäck, L. Hallstadius, Detailed analysis of the microstructure of the metal/oxide interface region in Zircaloy-2 after autoclave corrosion testing, ASTM Spec. Tech. Publ. 1529 STP (2011) 595–617, doi:10.1520/JAI102956.

[51] M. Preuss, P. Frankel, S. Lozano-Perez, D. Hudson, E. Polatidis, N. Ni, J. Wei, C. English, S. Storer, K.B. Chong, M. Fitzpatrick, P. Wang, J. Smith, C. Grovenor, G. Smith, J. Sykes, B. Cottis, S. Lyon, L. Hallstadius, R.J. Comstock, A. Ambard, M. Blat-Yrieix, Studies regarding corrosion mechanisms in zirconium alloys, ASTM Spec. Tech. Publ. 1529 (2011) 649–681 STP, doi:10.1520/stp49376t.

[52] Y. Dong, A.T. Motta, E.A. Marquis, Atom probe tomography study of alloying element distributions in Zr alloys and their oxides, J. Nucl. Mater. 442 (2013) 270–281, doi:10.1016/j.jnucmat.2013.08.055.

[53] B. Wadman, H.-.O. Andren, L.K.L. Falk, Atom Probe Analysis of Thin Oxide Layers on Zircaloy Needles, Le J. Phys. Colloq. 50 (1989) C8-303-C8-308, doi:10.1051/jphyscol:1989851.

[54] Y. Ichikawa, R. Tokoro, M. Tanno, K. Ogawa, Elucidation of cold-spray deposition mechanism by auger electron spectroscopic evaluation of bonding interface oxide film, Acta Mater. 164 (2019) 39–49, doi:10.1016/j.actamat.2018.09.041.

[55] Y. Li, Y. Wei, X. Luo, C. Li, N. Ma, Correlating particle impact condition with microstructure and properties of the cold-sprayed metallic deposits, J. Mater. Sci. Technol. 40 (2020) 185–195, doi:10.1016/j.jmst.2019.09.023.

[56] X.T. Luo, Y. Ge, Y. Xie, Y. Wei, R. Huang, N. Ma, C.S. Ramachandran, C.J. Li, Dynamic evolution of oxide scale on the surfaces of feed stock particles from cracking and segmenting to peel-off while cold spraying copper powder having a high oxygen content, J. Mater. Sci. Technol. 67 (2021) 105–115, doi:10.1016/j.jmst.2020.06.019.

[57] P.C. King, S.H. Zahiri, M. Jahedi, Focused ion beam micro-dissection of cold-sprayed particles, Acta Mater. 56 (2008) 5617–5626, doi:10.1016/j.actamat.2008.07.034.

[58] G.W. Chinthaka Silva, A.A. Kercher, J.D. Hunn, R.C. Martin, G.E. Jellison, H.M. Meyer, Characterization of zirconium carbides using electron microscopy, optical anisotropy, Auger depth profiles, X-ray diffraction, and electron density calculated by charge flipping method, J. Solid State Chem. 194 (2012) 91–99, doi:10.1016/j.jssc.2012.04.047.

[59] C.J. Li, W.Y. Li, Y.Y. Wang, Formation of metastable phases in cold-sprayed soft metallic deposit, Surf. Coatings Technol. 198 (2005) 469–473, doi:10.1016/j.surfcoat.2004.10.063.

[60] P. Perrot, M. Materials Science International Team, Cr-Zr Binary Phase Diagram Evaluation - Phase diagrams, crystallographic and thermodynamic data: Datasheet from MSI Eureka in, SpringerMaterials (2002) https://materials.springer.com/msi/docs/sm_msi_r_20_015393_01.

[61] K. Vieregge, C. Herzig, Grain boundary diffusion in α-zirconium. Part I: self-diffusion, J. Nucl. Mater. 173 (1990) 118–129, doi:10.1016/0022-3115(90)90250-Q.
[62] K. Vieregge, C. Herzig, Grain boundary diffusion in α-zirconium. Part II: fast diffusing cobalt bulk interstitials, J. Nucl. Mater. 175 (1990) 29–41, doi:10.1016/0022-3115(90)90266-P.
[63] P. Tejland, H.O. Andrén, G. Sundell, M. Thuvander, B. Josefsson, L. Hallstadius, M. Ivermark, M. Dahlbäck, Oxidation mechanism in zircaloy-2 - The effect of SPP size distribution, ASTM Spec. Tech. Publ. (2015) 373–403, doi:10.1520/STP154320130052.
[64] G.M. Hood, R.J. Schultz, Ultra-fast solute diffusion in α-Ti and α-Zr, Philos. Mag. 26 (1972) 329–336, doi:10.1080/14786437208227431.
[65] R.V. Patil, G.P. Tiwari, B.D. Sharma, Self-diffusion in Zr-Cr and Zr-Fe alloys, Philos. Mag. A Phys. Condens. Matter, Struct. Defects Mech. Prop. 44 (1981) 717–733, doi:10.1080/01418618108236174.
[66] G.M. Hood, R.J. Schultz, Tracer diffusion in α-Zr, Acta Metall. 22 (1974) 459–464, doi:10.1016/0001-6160(74)90098-4.
[67] J. Askill, D.H. Tomlin, Self-diffusion in chromium, Philos. Mag. 11 (1965) 467–474, doi:10.1080/14786436508224234.
[68] X.-.T. Luo, C.-.X. Li, F.-.L. Shang, G.-.J. Yang, Y.-.Y. Wang, C.-.J. Li, High velocity impact induced microstructure evolution during deposition of cold spray coatings: a review, Surf. Coatings Technol. 254 (2014) 11–20, doi:10.1016/J.SURFCOAT.2014.06.006.
[69] K.D. Ralston, N. Birbilis, Effect of grain size on corrosion: a review, Corrosion 66 (2010) 0750051–07500513, doi:10.5006/1.3462912.
[70] C. Suryanarayana, Nanocrystalline materials, Int. Mater. Rev. 40 (1995) 41–63, doi:10.1179/imr.1995.40.2.41.